B. Bouzidi[1],
B. El Badsi[2],
A. Masmoudi[3,*]

J. Electrical Systems 9-3 (2013): 367-379

Regular paper

Journal of Electrical Systems

Sensorless DTC strategy devoted to the control of FSTPI fed induction motor drives

The paper is aimed at the performance analysis of a sensorless direct torque control (DTC) strategy dedicated to four-switch three-phase inverter (FSTPI) fed induction motor (IM) drives. This strategy has been considered in an attempt to improve induction motor drive reliability, compactness and cost-effectiveness, which represent crucial requirements in electric and hybrid propulsion systems. These requirements could be achieved thanks to the substitution of the conventional six-switch three-phase inverter (SSTPI) by the reduced structure four-switch three-phase inverter (FSTPI). A model reference adaptive system (MRAS)-based speed estimator has been found suitable for the proposed sensorless DTC strategy in so far as it involves the same induction motor model, that is the *Clarke* model. It has been found through simulation work that the introduced sensorless DTC strategy exhibits high performance during transient and steady state operations.

Keywords: Sensorless direct torque control strategy; induction motor; four-switch three-phase inverter; reliability; compactness; cost-effectiveness; simulation.

1. Introduction

Recently, there is an increasing trend to improve the reliability, cost-effectiveness and compactness of electric machine drives which are crucial requirements in large scale production industries. The above-cited requirements could be fulfilled considering:

- the implementation of sensorless direct torque control (DTC) strategies with the encoder discarded, which exhibit attractive performance in terms of fast torque dynamic allied to simple implementation schemes [1, 2, 3].
- the substitution of conventional six-switch three-phase inverters (SSTPI) by reduced structure four-switch three-phase inverters (FSTPI), where the number of the power switches is taken down from six to four [4, 5, 6].

Over the last decade, many R&D projects focusing on the speed estimation of the induction motors are developed. So, different approaches have been reported in the literature in an attempt to achieve reliable high-performance direct torque-controlled drives [7, 8, 9]. Among the major developed induction motor speed estimators, one can distinguish the following ones:

- extended *Kalman* filter [1, 2].
- open-loop estimators [10].
- adaptive observers [11].
- estimators using either saliency effects or spatial saturation stator third harmonic voltage [1, 10].
- estimators using artificial intelligence, in particular neural networks and fuzzy logic systems [12].
- estimators based on the model reference adaptive system (MRAS) method [13].

[3,*] Corresponding author: Professor A. Masmoudi, Laboratory of Renewable Energies and Electric Vehicles, Department of Electromechanical Engineering, Sfax Engineering School, University of Sfax, 3038 Sfax, Tunisia, E-mail: a.masmoudi@enis.rnu.tn
[1] Laboratory of Renewable Energies and Electric Vehicles, Department of Electromechanical Engineering, Sfax Engineering School, University of Sfax, 3038 Sfax, Tunisia, E-mail: badiibouzidi2010@yahoo.fr
[2] Laboratory of Renewable Energies and Electric Vehicles, Department of Electromechanical Engineering, Sfax Engineering School, University of Sfax, 3038 Sfax, Tunisia, E-mail: bassemelbedsi@yahoo.fr

The implementation of the MRAS-based speed estimator has been selected in so far as it involves the same induction motor model as the one considered in the DTC strategies, that is the *Clarke* model.
Within these trends, the paper is aimed to the presentation of a sensorless DTC strategy dedicated to the control of reduced structure inverter FSTPI fed induction motor drives. A special attention is paid to the synthesis of the vector selection table and the dynamic and steady-state performance of the FSTPI fed induction motor drive are investigated through simulation works.

2. Principle of operation of FSTPI fed induction motor drives

The basic scheme of a FSTPI fed induction motor drive is illustrated in figure 1. The reduced structure FSTPI consists of a two-leg topology with two power switches per leg instead of three legs in the case of the conventional SSTPI. We consider the case where the FSTPI is feeding a three-phase induction motor with Y-connected phases. The two phases of the three-phase load are fed through the FSTPI legs, while the third phase is connected to the middle point of the DC-link voltage.

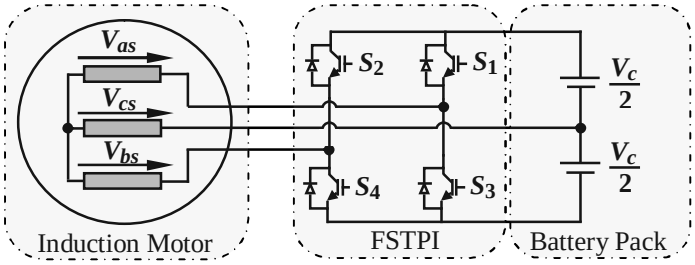

Figure 1: Connections of FSTPI fed induction motor drive

Let us assume that the states of the four power switches are denoted by the binary variables S_1 to S_4, where binary "1" corresponds to an ON state and the binary "0" indicates an OFF state. The states of the upper and lower switches of a leg are controlled complementary, which yields:

$$\begin{cases} S_3 = 1 - S_1 \\ S_4 = 1 - S_2 \end{cases} \tag{1}$$

The voltages across the induction motor phases can be expressed in terms of the two upper power switches states (S_1 and S_2) as follows:

$$\begin{cases} V_{as} = \dfrac{V_c}{6}(4S_1 - 2S_2 - 1) \\ V_{bs} = \dfrac{V_c}{6}(-2S_1 + 4S_2 - 1) \\ V_{cs} = \dfrac{V_c}{3}(-S_1 - S_2 + 1) \end{cases} \tag{2}$$

The application of the *Clarke* transform of the three phase voltages given by (2) yields the direct and quadrature components $V_{\alpha s}$ and $V_{\beta s}$ of the stator voltage vector, such that:

$$\begin{bmatrix} V_{\alpha s} \\ V_{\beta s} \end{bmatrix} = \sqrt{\frac{2}{3}} \begin{bmatrix} 1 & -\frac{1}{2} & -\frac{1}{2} \\ 0 & \frac{\sqrt{3}}{2} & -\frac{\sqrt{3}}{2} \end{bmatrix} \begin{bmatrix} V_{as} \\ V_{bs} \\ V_{cs} \end{bmatrix} \quad (3)$$

Four combinations of the states of the inverter power switches are characterized by four stator voltage vectors in the *Clarke* plane as shown in Figure 2. Table 1 summarizes these combinations and the corresponding voltages.

Table 1: Different combinations of the states of the FSTPI power switches and the corresponding voltage vectors located in the *Clarke* plane

S_1	S_2	V_{as}	V_{bs}	V_{cs}	$V_{\alpha s}$	$V_{\beta s}$	$\overline{V}$
0	0	$-\frac{V_c}{6}$	$-\frac{V_c}{6}$	$\frac{V_c}{3}$	$-\frac{V_c}{2\sqrt{6}}$	$-\frac{V_c}{2\sqrt{2}}$	$\overline{V_1}$
1	0	$\frac{V_c}{2}$	$-\frac{V_c}{2}$	0	$\frac{3V_c}{2\sqrt{6}}$	$-\frac{V_c}{2\sqrt{2}}$	$\overline{V_2}$
1	1	$\frac{V_c}{6}$	$\frac{V_c}{6}$	$-\frac{V_c}{3}$	$\frac{V_c}{2\sqrt{6}}$	$\frac{V_c}{2\sqrt{2}}$	$\overline{V_3}$
0	1	$-\frac{V_c}{2}$	$\frac{V_c}{2}$	0	$-\frac{3V_c}{2\sqrt{6}}$	$\frac{V_c}{2\sqrt{2}}$	$\overline{V_4}$

Referring to figure 2, one can notice that the four voltage vectors are shifted by $\frac{\pi}{2}$. Furthermore, it is to be noted that vectors $\overline{V}_1$ and $\overline{V}_3$ have an amplitude equal to $\frac{V_c}{\sqrt{6}}$, while vectors voltage $\overline{V}_2$ and $\overline{V}_4$ have an amplitude equal to $\frac{V_c}{\sqrt{2}}$. The location of the four voltage vectors in the *Clarke* plane defines the four sectors.

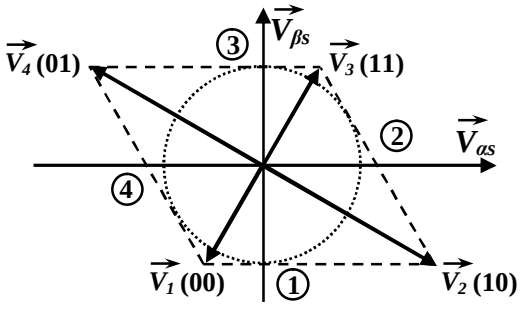

Figure 2: FSTPI output voltage vectors located in the *Clarke* plane

3. Direct torque control of a FSTPI fed induction motor drive

The scheme of the proposed DTC strategy dedicated to the control of FSTPI fed induction motor drives is illustrated in figure 3. It is built around three loops, which are:

- the speed loop including a PI controller, whose output yields the reference electromagnetic torque,
- the electromagnetic torque loop including a three-level hysteresis regulator. It provides the control signal c_Γ which takes the states +1, 0 or -1 to increase, maintain or decrease the torque, respectively,
- the stator flux loop including a two-level hysteresis regulator. It gives the control signal c_φ which takes the states +1 or 0 to increase or decrease the flux, respectively.

The stator flux vector can be expressed as:

$$\frac{d}{dt}\overline{\Phi}_s = \overline{V}_s - r_s \overline{I}_s \tag{4}$$

If the voltage drop across the stator resistance is neglected, equation (4) yields:

$$\Delta\overline{\Phi}_s = \overline{\Phi}_s(K+1) - \overline{\Phi}_s(K) \approx \overline{V}_s T_s \tag{5}$$

Where T_s is the sampling period and where $\overline{\Phi}s(K)$ and $\overline{\Phi}s(K+1)$ are the stator flux vectors at instants KT_s and $(K+1)T_s$.
This means that the flux variation is held by the stator voltage phasor direction [13].
Figure 4 illustrates a case of variation of the stator flux vector after a sampling period T_s.
The amplitude and phase of the stator flux vector are expressed using *Clarke* variables as follows:

$$\begin{cases} \Phi_s = \sqrt{\phi^2{}_{\alpha s} + \phi^2{}_{\beta s}} \\ \theta_s = \arctan\left(\dfrac{\phi_{\beta s}}{\phi_{\alpha s}}\right) \end{cases} \tag{6}$$

where:

$$\begin{cases} \phi_{\alpha s} = \int (V_{\alpha s} - r_s i_{\alpha s})dt \\ \phi_{\beta s} = \int (V_{\beta s} - r_s i_{\beta s})dt \end{cases} \tag{7}$$

The electromagnetic torque can be expressed in terms of stator current and flux as follows:

$$T_{em} = N_p(\phi_{\alpha s} i_{\beta s} - \phi_{\beta s} i_{\alpha s}) \tag{8}$$

where N_p is the pole pair number.

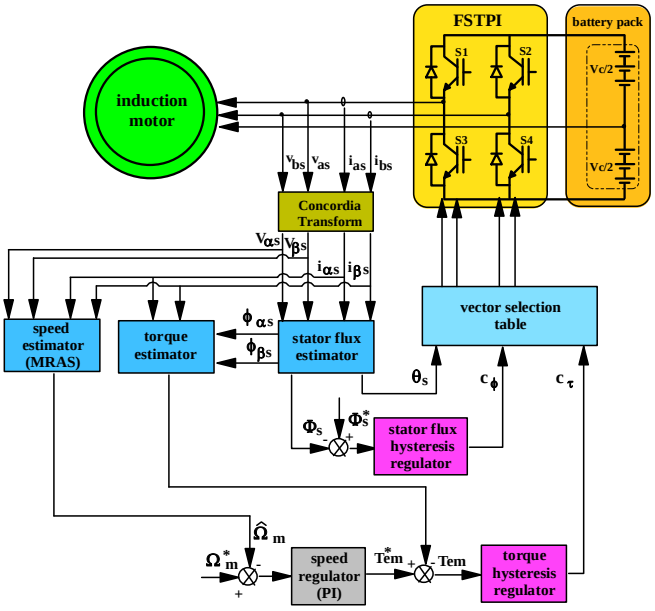

Figure 3: Bloc diagram of a dedicated sensorless DTC strategy

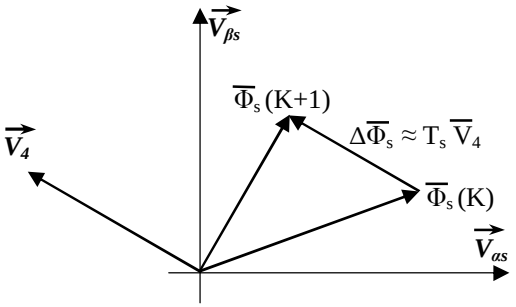

Figure 4: Evolution of the flux vector in the *Clarke* plane after a sampling period T_s

In the *Clarke* plane, the FSTPI provides only four active vectors. In this case, this plane is divided into four sectors as shown in figure 2. Giving the reduced number of the active voltage vectors, we have been involved in the subdivision of this plane through the synthesis of virtual active vectors in order to reach a high dynamic with reduced torque ripple. Following different trials, these requirements have been fulfilled thanks to the introduction of four virtual vectors as shown in figure 5.

Let us call $\overline{V}_1$, $\overline{V}_3$, $\overline{V}_5$ and $\overline{V}_7$ the basic active vectors. Referring to figure 5, the virtual vectors $\overline{V}_2$, $\overline{V}_4$, $\overline{V}_6$ and $\overline{V}_8$ represent the half of the sum of the adjacent basic vectors. Therefore, applying one of the virtual vectors is equal to applying two adjacent basic vectors during two sampling periods ($2T_s$).

Within this approach, the *Clarke* plane would normally be divided into eight sectors as illustrated in figure 5. Nevertheless, it has been noticed that in large sectors, the application of the corresponding active vectors gives different results depending on the position of the flux vector in the sector. Therefore, the introduction of further sub-sectors turns to be necessary. Therefore, the large sectors (first and fifth) of figure 5 have been subdivided into four sub-sectors each, while the remaining sectors have been subdivided into two sub-sectors each.So, the *Clarke* plane turns to be subdivided into twenty sectors as illustrated in figure 6.

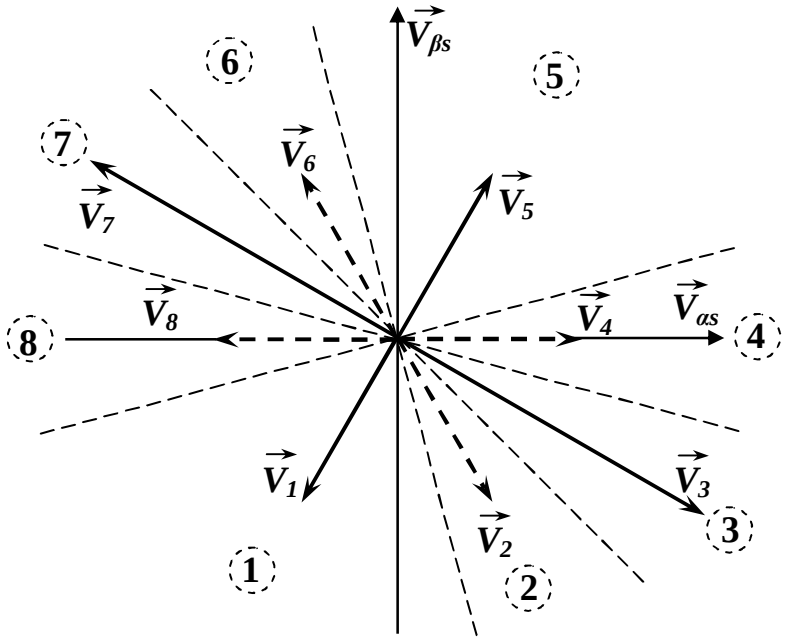

Figure 5: Basic and virtual active voltage vectors

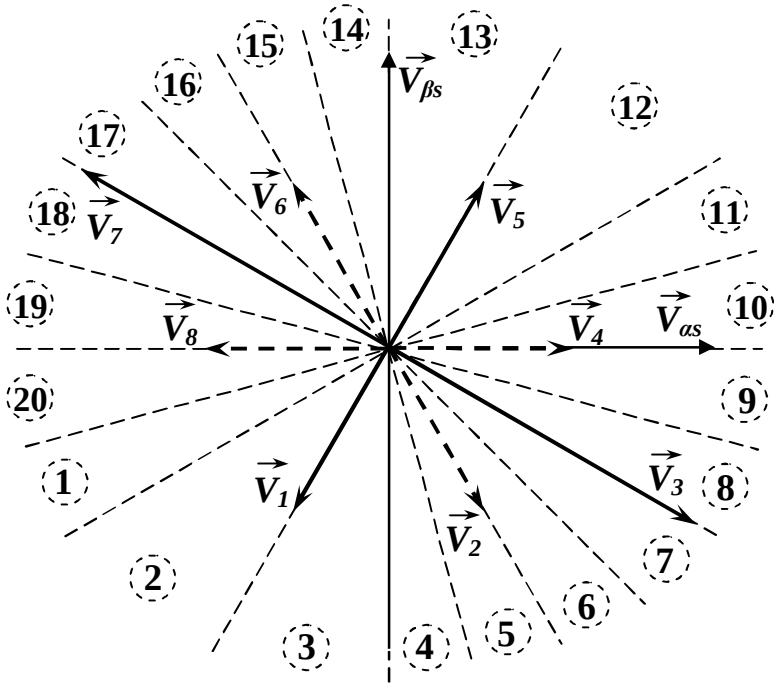

Figure 6: Subdivision of the *Clarke* plane into twenty sectors

The most critical issue is how to substitute the "null-vector", in order to achieve the control signals in the case of maintaining the torque. It has been found that this could be achieved by applying two opposite vectors among ($\overline{V}_1$ and $\overline{V}_5$) or ($\overline{V}_3$ and $\overline{V}_7$) in order to compensate the corresponding effects in the sectors non-adjacent to the basic vectors.
Many possibilities could be chosen in selecting the combinations of the voltage vectors. After many trials, we have adopted the vector selection table presented in table 2.

Table 2: Vector selection table of the proposed DTC strategy

c_ϕ	+1	+1	+1	0	0	0
c_Γ	+1	0	-1	+1	0	-1
S_1	$\overline{V}_1$	$\overline{V}_1/\overline{V}_5$	$\overline{V}_7$	$\overline{V}_3$	$\overline{V}_1/\overline{V}_5$	$\overline{V}_5$
S_2	$\overline{V}_2$	$\overline{V}_1$	$\overline{V}_8$	$\overline{V}_3$	$\overline{V}_5$	$\overline{V}_5$
S_3	$\overline{V}_2$	$\overline{V}_1$	$\overline{V}_8$	$\overline{V}_4$	$\overline{V}_5$	$\overline{V}_6$
S_4	$\overline{V}_3$	$\overline{V}_1/\overline{V}_5$	$\overline{V}_1$	$\overline{V}_4$	$\overline{V}_1/\overline{V}_5$	$\overline{V}_6$
S_5	$\overline{V}_3$	$\overline{V}_1/\overline{V}_5$	$\overline{V}_1$	$\overline{V}_5$	$\overline{V}_1/\overline{V}_5$	$\overline{V}_7$
S_6	$\overline{V}_4$	$\overline{V}_1/\overline{V}_5$	$\overline{V}_1$	$\overline{V}_5$	$\overline{V}_1/\overline{V}_5$	$\overline{V}_7$
S_7	$\overline{V}_4$	$\overline{V}_3$	$\overline{V}_1$	$\overline{V}_5$	$\overline{V}_7$	$\overline{V}_8$
S_8	$\overline{V}_5$	$\overline{V}_3$	$\overline{V}_2$	$\overline{V}_5$	$\overline{V}_7$	$\overline{V}_8$
S_9	$\overline{V}_5$	$\overline{V}_1/\overline{V}_5$	$\overline{V}_2$	$\overline{V}_6$	$\overline{V}_1/\overline{V}_5$	$\overline{V}_1$
S_{10}	$\overline{V}_5$	$\overline{V}_1/\overline{V}_5$	$\overline{V}_3$	$\overline{V}_6$	$\overline{V}_1/\overline{V}_5$	$\overline{V}_1$
S_{11}	$\overline{V}_5$	$\overline{V}_1/\overline{V}_5$	$\overline{V}_3$	$\overline{V}_7$	$\overline{V}_1/\overline{V}_5$	$\overline{V}_1$
S_{12}	$\overline{V}_6$	$\overline{V}_5$	$\overline{V}_4$	$\overline{V}_7$	$\overline{V}_1$	$\overline{V}_1$
S_{13}	$\overline{V}_6$	$\overline{V}_5$	$\overline{V}_4$	$\overline{V}_8$	$\overline{V}_1$	$\overline{V}_2$
S_{14}	$\overline{V}_7$	$\overline{V}_1/\overline{V}_5$	$\overline{V}_5$	$\overline{V}_8$	$\overline{V}_1/\overline{V}_5$	$\overline{V}_2$
S_{15}	$\overline{V}_7$	$\overline{V}_1/\overline{V}_5$	$\overline{V}_5$	$\overline{V}_1$	$\overline{V}_1/\overline{V}_5$	$\overline{V}_3$
S_{16}	$\overline{V}_8$	$\overline{V}_1/\overline{V}_5$	$\overline{V}_5$	$\overline{V}_1$	$\overline{V}_1/\overline{V}_5$	$\overline{V}_3$
S_{17}	$\overline{V}_8$	$\overline{V}_7$	$\overline{V}_5$	$\overline{V}_1$	$\overline{V}_3$	$\overline{V}_4$
S_{18}	$\overline{V}_1$	$\overline{V}_7$	$\overline{V}_6$	$\overline{V}_1$	$\overline{V}_3$	$\overline{V}_4$
S_{19}	$\overline{V}_1$	$\overline{V}_1/\overline{V}_5$	$\overline{V}_6$	$\overline{V}_2$	$\overline{V}_1/\overline{V}_5$	$\overline{V}_5$
S_{20}	$\overline{V}_1$	$\overline{V}_1/\overline{V}_5$	$\overline{V}_7$	$\overline{V}_2$	$\overline{V}_1/\overline{V}_5$	$\overline{V}_5$

4. MRAS based speed estimator

The MRAS approach has been introduced in 1992 by *Schauder* [14]. Since then, it has been the subject of many researches focused on sensorless control strategies of induction motor drives [15].
As shown in figure 7, the MRAS-based speed estimation consists in an adaptive procedure built around the comparison between the outputs of two models which are derived from the induction motor equations expressed in the *Clarke* plane:

- the reference model which is independent of the speed. This model considers the estimated rotor flux derived from the stator equation, as follows:

$$\begin{cases} \phi_{\alpha r} = \dfrac{l_r}{M}\left[\int (V_{\alpha s} - r_s i_{\alpha s})\, dt - \sigma\, l_s\, i_{\alpha s}\right] \\ \phi_{\beta r} = \dfrac{l_r}{M}\left[\int (V_{\beta s} - r_s i_{\beta s})\, dt - \sigma\, l_s\, i_{\beta s}\right] \end{cases} \tag{9}$$

- the adaptive model which depends of the speed. This model considers the estimated rotor flux derived from the rotor equation, leading to the following:

$$\begin{cases} \hat{\phi}_{\alpha r} = \int \left(M\, \beta_r\, i_{\alpha s} - \beta_r\, \hat{\phi}_{\alpha r} - \hat{\omega}_m\, \hat{\phi}_{\beta r}\right) dt \\ \hat{\phi}_{\beta r} = \int \left(M\, \beta_r\, i_{\beta s} - \beta_r\, \hat{\phi}_{\beta r} + \hat{\omega}_m\, \hat{\phi}_{\alpha r}\right) dt \end{cases} \tag{10}$$

where $\beta_r = \dfrac{r_r}{l_r}$

The expression of the speed error ε_ω, obtained from the comparison between both reference and adaptive models, is expressed as follows:

$$\varepsilon_\omega = \hat{\phi}_{\alpha r}\, \phi_{\beta r} - \phi_{\alpha r}\, \hat{\phi}_{\beta r} \tag{11}$$

The adaptive mechanism generates the value of the estimated speed $\hat{\omega}_m$ by minimizing ε_ω. This is carried out considering a PI controller generating the estimated speed $\hat{\omega}_m$ which is fed back to the adaptive model.

The estimated speed is expressed as follows:

$$\hat{\omega}_m = \left(k_p + \frac{k_i}{s}\right) \varepsilon_\omega \tag{12}$$

The application of the *Popov's* hyperstability criterion is considered in order to achieve the convergence of the MRAS.

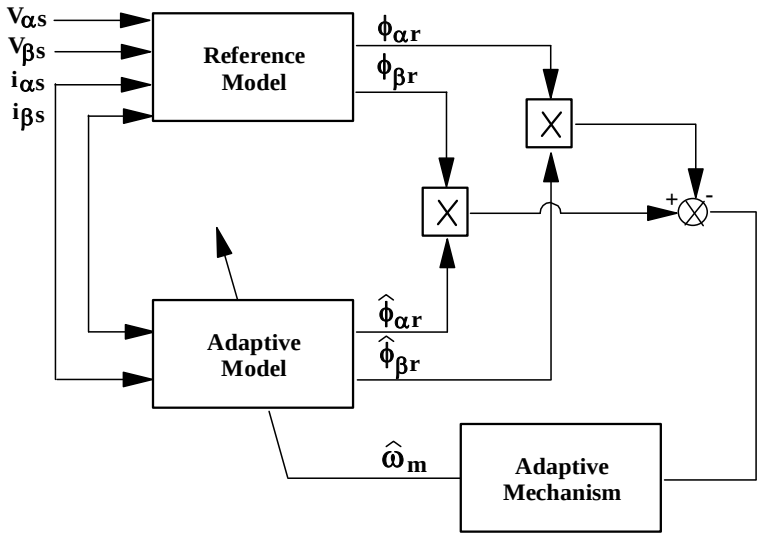

Figure 7: MRAS speed estimator

5. Simulation

In order to investigate the performance of the FSTPI fed induction motor drives under the control of the proposed sensorless DTC strategy, simulation works have been carried out in the MATLAB-SIMULINK environment.
The induction motor ratings and parameters are given in tables 3 and 4, respectively.

Table 3: Ratings of the induction motor

Power	0.37 KW	Efficiency	77%
Voltage	230V / 400V	Current	1.7A / 1A
Torque	2.56 N.m	Stator flux (rms)	640 mWb
Speed	1380 rpm	Frequency	50 Hz

Table 4: Parameters of the induction motor

r_s = 24.6 Ω	r_r = 17.9 Ω
ls = 984 mH	lr = 984 mH
M = 914 mH	Np = 2
J = 2.5 g.m^2	f = 0.006 N.m.S

A DC-link voltage of 600V has been considered. The flux hysteresis band has been taken equal to 0.01Wb which represents 1% of the rated value of the stator flux. The hysteresis band of the torque regulator has been chosen equal to 0.02N.m which represents 0.8% of the rated electromagnetic torque.

The reference speed varies versus time according to the waveform described below:

- an acceleration from 0 to 300rpm during 0.2s,
- from 0.2s to 0.5s, the reference speed is taken constant equal to 300rpm,
- a negative step characterized by a speed reversal from 300rpm to -300rpm at 0.9s,
- from 0.9s to 1s, the reference speed is kept constant equal to -300rpm.

In what follows, we consider the transient and steady-state performances of the induction motor drive considering a constant load torque T_L = 0.5N.m. The obtained results are shown in figures 8 and 9.

Figures 8.a shows the evolution of the reference speed and the MRAS estimated one versus time. Referring to these waveforms, one can notice the high performance of the speed estimator.

Figures 8.b illustrates a zoom of the MRAS estimated speed and its reference versus time corresponding to the steady-state operation. It's to be noted that the MRAS speed reaches its reference with an error which does not exceed 0.7%.

From the analysis of figure 8.c illustrating the variations of the electromagnetic torque with respect to time, one can confirm that the sensorless DTC strategy offers high torque dynamics.

Figure 8.d shows the evolution of the reference and the stator flux amplitudes versus time. This result confirms the high dynamic of the flux control loops offered by the proposed strategy.

Figure 8.e and figure 9.a, illustrate the stator current of the phase connected to a leg of the FSTPI and the one of the phase linked to the middle point of the DC bus voltage, respectively. These currents present a quite reasonable harmonic content. As expected, one can notice the presence of a perturbation in these waveforms during the speed reversal.

Figure 8.f and figure 9.b, show the stator voltage of the phase connected to a leg of the FSTPI and the one of the phase linked to the middle point of the DC bus voltage, respectively. One can notice that the phase voltages present asymmetrical waveforms.

Figure 9.c shows the α- and β-components of the stator flux with respect to time. One can notice the high dynamic behavior of these components in both transient and steady-state operations. It is to be noted also that these components of the stator flux present almost the same amplitude which is equal to the module of the flux reference.

The locus of the extremities of the stator voltage vector in the *Clarke* plane is illustrated in figure 9.d. This latter presents a lozenge-shape and confirms the application of the four voltage vectors generated by the FSTPI.

Figure 9.e illustrates the sector successions in the case of the sensorless DTC strategy. It is to be noted that there are twenty commutations during each stator period.

Finally, for the sake of further investigation of the stator flux dynamic, the locus described by the extremity of its vector in the *Clarke* plane is shown in figure 9.f. It is to be noted that the locus of the extremity of the stator flux vector is smooth and has a circular shape.

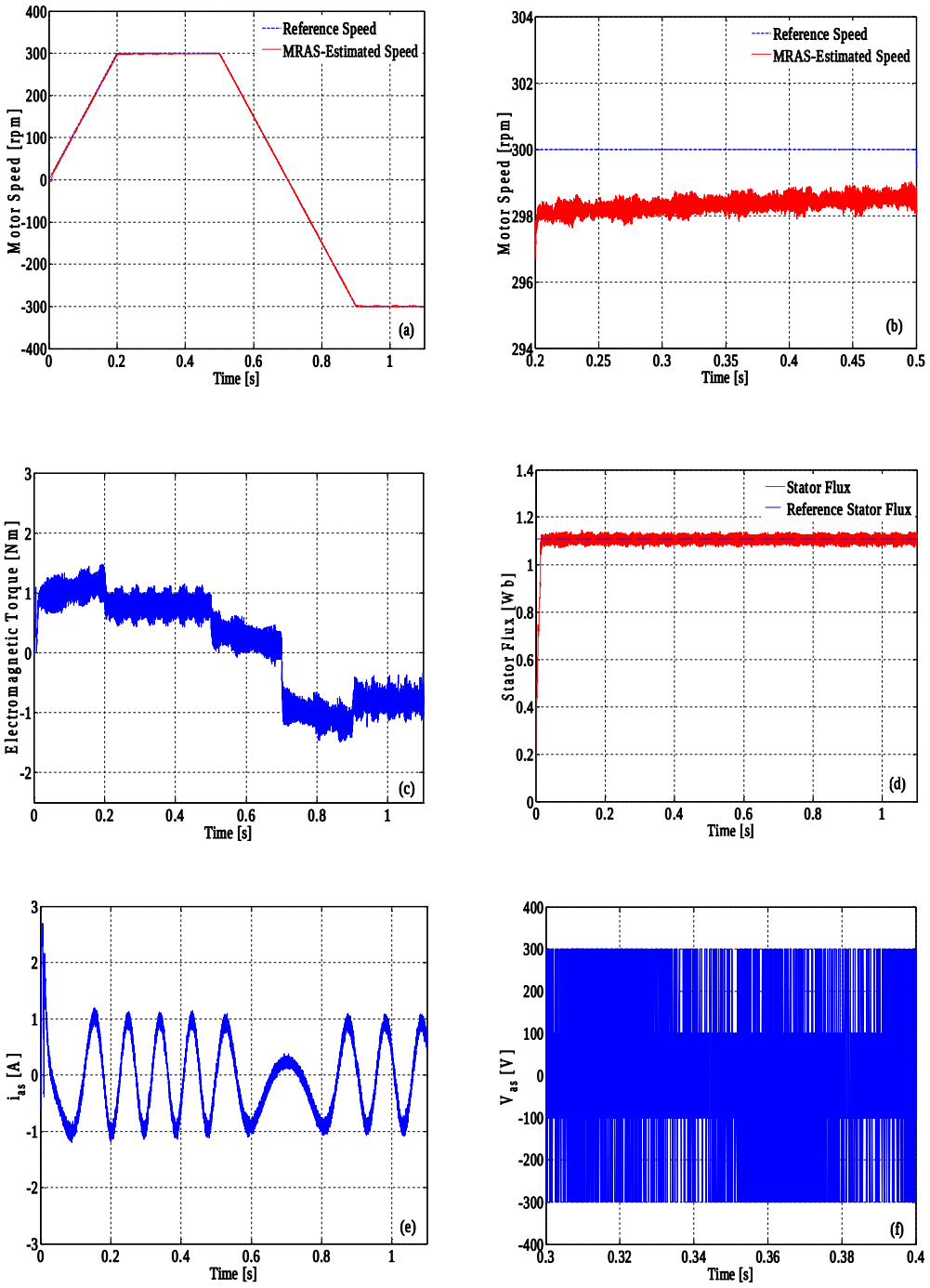

Figure 8: Simulation results corresponding to the performance of the IM drive under the sensorless DTC strategy at load operation. Legend: (a) MRAS estimated speed and its reference, (b) zoom of the MRAS speed and the reference one, (c) electromagnetic torque, (d) stator flux and its reference, (e) stator current of a phase connected to a leg of the FSTPI, (f) stator voltage of a phase connected to a leg of the FSTPI

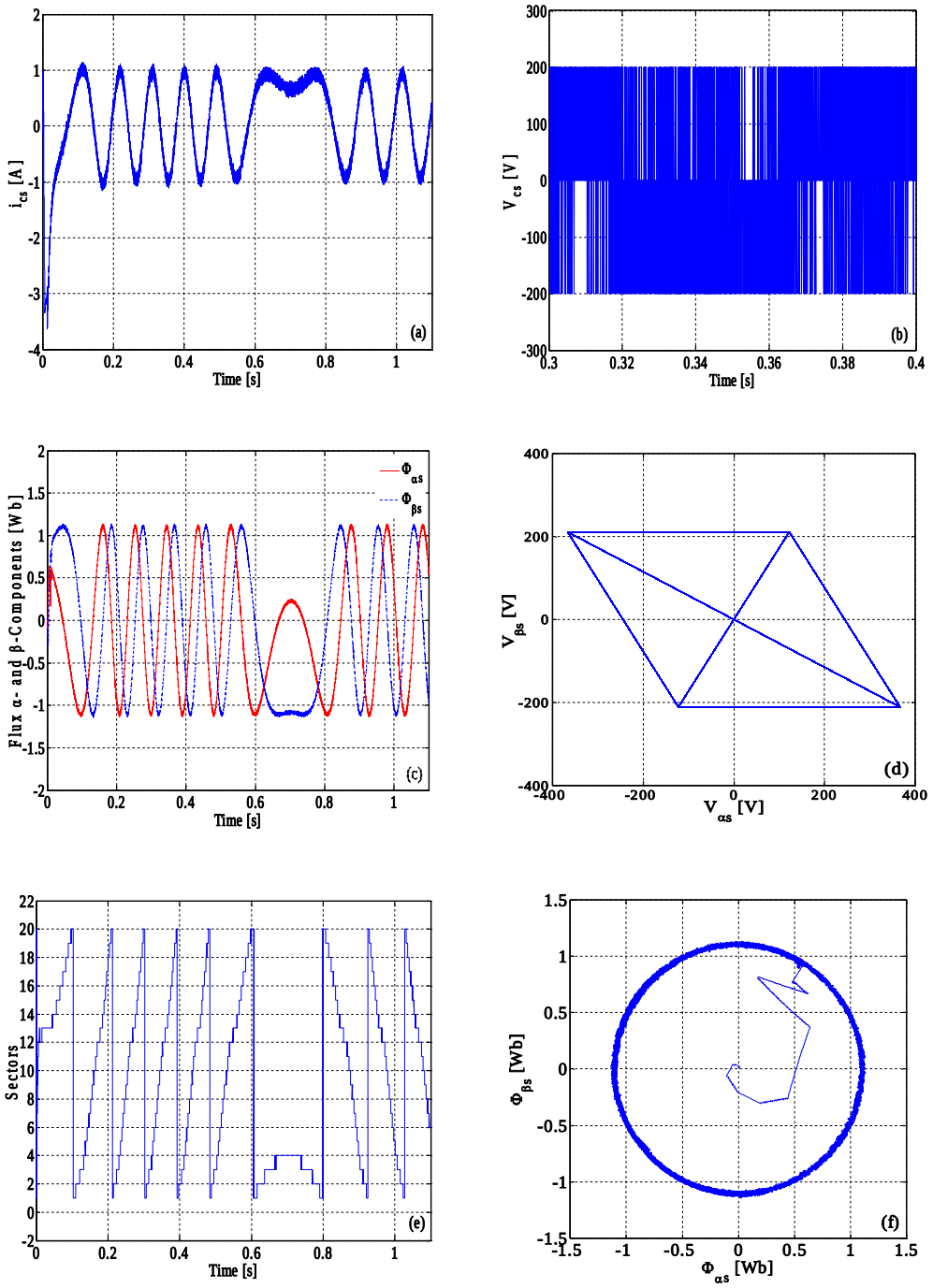

Figure 9: Simulation results corresponding to the performance of the IM drive under the sensorless DTC strategy at load operation. Legend: (a) stator current of the phase linked to the middle point of the DC bus voltage, (b) stator voltage of the phase linked to the middle point of the DC bus voltage, (c) α- and β-components of $\overline{\Phi}_s$, (d) α- and β-components of $\overline{V}_s$, (e) sector successions, (f) locus of the extremities of $\overline{\Phi}_s$ in the *Clarke* plane

6. Conclusion

This work is devoted to the performance analysis of a sensorless direct torque control strategy dedicated to four-switch three-phase inverter (FSTPI) fed induction motor drives. This strategy has been considered in an attempt to improve induction motor drive reliability, compactness and cost-effectiveness, integrated in electric and hybrid propulsion systems. These requirements have been achieved thanks to the substitution of the conventional inverter by the reduced structure FSTPI one. A model reference adaptive system (MRAS)-based speed estimator has been found suitable for the proposed sensorless DTC strategy. Finally, it has been found through simulation work that the introduced DTC strategy exhibits high performance during transient and steady state operations. It has been found that FSTPI inverter fed induction motor drives under the control of the proposed DTC strategy could be viable candidates in low-cost applications.

Acknowledgment

This work was financed by the Ministry of Higher Education and Scientific Research, Tunisia.

References

[1] Y. Zhang, J. Zhu, Z. Zhao, W. Xu, and D. G. Dorrell, An improved direct torque control for three-level inverter-fed induction motor sensorless drive, *IEEE Transactions on Power Electronics*, 27(3), 1502-1513, 2012.

[2] Q. T. An, L. Z. Sun, K. Zhao, and L. Sun, Switching function model based fast-diagnostic method of open-switch faults in inverters without sensors, *IEEE Transactions on Power Electronics*, 26(1), 119-126, 2011.

[3] K. B. Lee, and F. Blaabjerg, Sensorless DTC-SVM for induction motor driven by a matrix converter using a parameter estimation strategy, *IEEE Transactions on Industrial Electronics*, 55(2), 512-521, 2008.

[4] B. El Badsi, B. Bouzidi, and A. Masmoudi, DTC scheme for a four-switch inverter-fed induction motor emulating the six-switch inverter operation, *IEEE Transactions on Power Electronics*, 28(7), 3528-3538, 2013.

[5] R. Wang, J. Zhao, and Y. Liu, A comprehensive investigation of four-switch three-phase voltage source inverter based on double fourier integral analysis, *IEEE Transactions on Power Electronics*, 26(10), 2774-2787, 2011.

[6] K. D. Hoang, Z. Q. Zhu, and M. P. Foster, Influence and compensation of inverter voltage drop in direct torque-controlled four-switch three-phase PM brushless AC drives, *IEEE Transactions on Power Electronics*, 26(8), 2343-2357, 2011.

[7] B. El Badsi, B. Bouzidi, and A. Masmoudi, Bus-clamping based DTC: an attempt to reduce harmonic distortion and switching losses, *IEEE Transactions on Power Electronics*, 60(3), 873-884, 2013.

[8] M. N. Uddin, and M. Hafeez, FLC-based DTC scheme to improve the dynamic performance of an IM drive, *IEEE Transactions on Industry Applications*, 48(2), 823-831, 2012.

[9] A. Taheri, A. Rahmati, and S. Kaboli, Efficiency improvement in DTC of six-phase induction machine by adaptive gradient descent of flux, *IEEE Transactions on Power Electronics*, 27(3), 1552-1562, 2012.

[10] K. L. Shi, T. F. Chan, Y. K. Wong, and S. L. Ho, Speed estimation of an induction motor drive using an optimized extended Kalman filter, *IEEE Transactions on Industrial Electronics*, 49(1), 124-133, 2004.

[11] J. Holtz, and J. Quan, Drift- and parameter-compensated flux estimator for persistent zero-stator-frequency operation of sensorless-controlled induction motors, *IEEE Transactions on Industrial Applications*, 39(4), 1052–1060, 2003.

[12] T. O. Kowalska, and M. Dybkowski, Stator current-based MRAS estimator for wide range speed-sensorless induction motor drive, *IEEE Transactions on Industrial Electronics*, 57(4), 1296-1308, 2010.

[13] S. H. Huh, K. B. Lee, D. W. Kim, I. Choy, and G. T. Park, Sensorless control of induction motor using a neural network for speed estimation, *International Journal of Control, Automation, and Systems*, 3(4), 612-619, 2005.

[14] C. Schauder, Adaptive speed identification for vector control of induction motors without rotational transducers, *IEEE Transactions on Industry Applications*, 28(5), 1054-1061, 1992.

[15] M. Hajian, J. Soltani, G. A. Markadeh, and S. Hosseinnia, Adaptive nonlinear direct torque control of sensorless IM drives with efficiency optimization, *IEEE Transactions Industrial Electronics*, 57(3), 975–985, 2010.